Calibration Method for ML Estimation of 3D Interaction Position in a Thick Gamma-Ray Detector

William C. J. Hunter, *Member, IEEE*, Harrison H. Barrett, *Fellow, IEEE*, and Lars R. Furenlid, *Member, IEEE*

***Abstract*—High-energy ($>$ 100 keV) photon detectors are often made thick relative to their lateral resolution in order to improve their photon-detection efficiency. To avoid issues of parallax and increased signal variance that result from random interaction depth, we must determine the 3D interaction position in the imaging detector. With this goal in mind, we examine a method of calibrating response statistics of a thick-detector gamma camera to produce a maximum-likelihood estimate of 3D interaction position. We parameterize the mean detector response as a function of 3D position, and we estimate these parameters by maximizing their likelihood given prior knowledge of the pathlength distribution and a complete list of camera signals for an ensemble of gamma-ray interactions. Furthermore, we describe an iterative method for removing multiple-interaction events from our calibration data and for refining our calibration of the mean detector response to single interactions. We demonstrate this calibration method with simulated gamma-camera data. We then show that the resulting calibration is accurate and can be used to produce unbiased estimates of 3D interaction position.**

***Index Terms*—3D interaction position, depth of interaction, gamma-ray imaging, mean detector response calibration, maximum likelihood estimation, multiple-hit event filtering.**

I. Introduction

DETECTORS used for high-energy photon detection are often made thick in order to improve their photon-detection efficiency. Use of a thick detector, in turn, motivates depth of interaction (DOI) estimation for each gamma ray. If we estimate only the two-dimensional (2D) position of interaction in a gamma camera, ambiguity in DOI may result in a loss of detector and/or image resolution [1]. Random DOI can cause increased signal variance, which in turn can degrade the 2D resolution of a gamma camera. Additionally, DOI ambiguity for obliquely incident gamma rays causes parallax, which can subsequently limit image resolution. Random DOI can also degrade coincidence-timing resolution for a time-of-flight PET system [2]. For many clinical gamma cameras with moderately thick scintillators ($<$ 10 mm), signal-variance and parallax issues are mitigated by choice of camera geometry and optical properties. However, to avoid these issues in general for a thicker gamma-ray detector, we must estimate the three-dimensional (3D) coordinates of interaction.

A variety of statistical methods for estimating DOI in a thick monolithic detector have been suggested [1], [3]–[5]. To make efficient use of information contained by the camera signals $\boldsymbol{g} = \{g_m, m = 1 \cdots M\}$, we determine the 3D interaction position $\boldsymbol{R} = \{x, y, z\}$ by maximum likelihood (ML) estimation [1], [6]:

$$\hat{\boldsymbol{R}}_{\mathrm{ML}} = \underset{\boldsymbol{R}}{\arg\max}\{\mathrm{pr}(\boldsymbol{g}|\,\boldsymbol{R}, E)\}. \tag{1}$$

Here, the operator $\arg\max$ returns the value of the indicated parameter that maximizes the operand, and the caret denotes a parameter estimate. The operand $\mathrm{pr}(\boldsymbol{g}|\boldsymbol{R}, E)$ is a probability model of $\boldsymbol{g}$ given $\boldsymbol{R}$ and energy E. However, interpreted as a function of the parameters $\boldsymbol{R}$ and/or E for given $\boldsymbol{g}$, $\mathrm{pr}(\boldsymbol{g}|\boldsymbol{R}, E)$ is called a likelihood function. An equivalent and often more convenient method for finding an ML estimate is to maximize the log likelihood $\ln[\mathrm{pr}(\boldsymbol{g}|\boldsymbol{R}, E)]$.

To find an ML estimate, we use a fast ML-search algorithm called a contracting-grid search, which is proposed by [7]. Our implementation of this search algorithm was on a 2.0-GHz dual-core AMD Athlon(tm) MP 2400+ processor. We were able to generate 3D ML estimates with 64 camera signals on a 69-by-69-by-25 grid at a rate of about 500 events/sec per processor. Faster implementations of this algorithm are being (or have been) developed for cell processors, GPUs, and FPGAs.

To simultaneously estimate 3D-position and energy, we calibrate $\mathrm{pr}(\boldsymbol{g}|\boldsymbol{R}, E)$ as a function of both $\boldsymbol{R}$ and E and then we find the ML estimate over this 4-dimensional space. However, as is discussed later [see (10)], the calibration of $\mathrm{pr}(\boldsymbol{g}|\boldsymbol{R}, E)$ is a separable task. In this paper, we assume E to be known and we estimate just $\boldsymbol{R}$; unlike clinical gamma-ray image acquisitions, we can produce a nearly monoenergetic gamma-ray beam for calibrating the detector response as a function of just $\boldsymbol{R}$. We can effectively remove non-photopeak calibration events using a statistical test (e.g., likelihood threshold) as we do later in Section I to remove multiple-interaction events. Furthermore, position estimates of non-photopeak events tend to be isolated at the boundaries of parameter space, where they are easily identified and filtered.

To generate the ML estimate of $\boldsymbol{R}$ for given $\boldsymbol{g}$, we must model $\mathrm{pr}(\boldsymbol{g}|\boldsymbol{R}, E)$, and we must calibrate representative statistics (e.g., the mean detector response) of this probability model as a function of $\boldsymbol{R}$ for given E. A straightforward procedure for calibrating detector-response statistics as a function of event parameters is to measure $\boldsymbol{g}$ for an ensemble of gamma rays for fixed

Manuscript received February 18, 2008; revised August 26, 2008. Current version published February 11, 2009. This work was supported in part by the U.S. National Institutes of Health NIBIB under Grant P41-EB002035.

W. C. J. Hunter was with the Department of Physics and the Department of Radiology, University of Arizona, Tucson, AZ 85724 USA. He is now with the Department of Radiology, University of Washington, Seattle, WA 98195 USA (e-mail: wcjh@u.washington.edu).

H. H. Barrett is with the Department of Radiology, the College of Optical Sciences, the Applied Mathematics Program, and the Biomedical Engineering Program, University of Arizona, Tucson, AZ 85724 USA (e-mail: hhb@email.arizona.edu).

L. R. Furenlid is with the Department of Radiology, the College of Optical Sciences, and the Biomedical Engineering Program, University of Arizona, Tucson, AZ 85724 USA (e-mail: furen@radiology.arizona.edu).

Digital Object Identifier 10.1109/TNS.2008.2010704

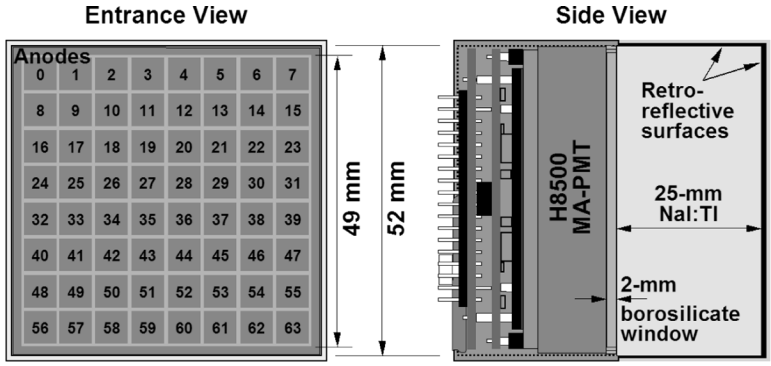

Fig. 1. Diagram of the simulated test camera. In this design, we assume that the entrance and edge surfaces are ideal retroreflectors, that the detector-window interface is optically diffuse, and that electronic and gain noise are negligible.

event parameters. For instance, the lateral interaction position and energy of a gamma ray are controlled by tightly collimating a known source. However, gamma-ray pathlength is beyond our control and remains a random variable.

In this work, we show how to use prior knowledge of the pathlength distribution and the set of observations for an ensemble of gamma-ray interactions to calibrate 3D model statistics. We demonstrate this method by simulation of signal generation and output from a monolithic-scintillator gamma camera. For this purpose, we use an open-source photon-transport Monte Carlo algorithm (SCOUT) described in Chapter 4 of [8].

II. Modeling $\mathrm{pr}(\boldsymbol{g}|\boldsymbol{R}, E)$

Scintillation-camera output signals, $\boldsymbol{g}$, in response to a gamma ray of energy E interacting at the position $\boldsymbol{R}$ result from a sequence of random processes: light production, light collection, photoelectric conversion, electronic amplification, and electronic readout. For this work, we consider the detector response to single-interaction (photoelectric) events in a thick scintillation camera with multi-anode photomultiplier tube (MA-PMT) optical readout (Fig. 1).

A. Light Production

The number of optical photons, N_{opt}, that result when a gamma ray of energy E deposits its energy in a scintillator is random. A general description of the distribution of N_{opt} is non-trivial (e.g., see [9]). Although there is some insight into the mechanisms that produce scintillation light [10], a precise description of the statistics for scintillation light does not exist. However, one observation that we can make by examining the energy resolution of a scintillator-based gamma-ray spectrometer is that the variance of N_{opt} tends to exceed that of a Poisson random variable of identical mean value [11].

In the next section, we find that collection and quantum efficiency of individual photodetectors play a much larger role in the signal statistics than does the scintillation process. Therefore, to simulate the detector response, we presently adopt a probability model for N_{opt} that accounts for the mean light yield and for the observed excess variance as a function of deposited energy. Specifically, we assume an energy-dependent normal random variable. For a deposited gamma-ray energy E, the mean number of optical photons produced is $\bar{N}_{\mathrm{opt}}(E)$, and the observed variance is $\mathrm{Var}(N_{\mathrm{opt}}|E)$. We use a nonnegativity constraint on this distribution, which rarely is invoked since the distribution width tends to be much smaller than the mean.

B. Light Collection and Photoelectric Conversion

Scintillation light is collected by an array of M photodetectors on the scintillator periphery. The fraction of scintillation light collected by the mth photodetector, $\eta_m(\boldsymbol{R})$, is a product of the geometric efficiency, $\alpha_m(\boldsymbol{R})$, and the quantum efficiency, β_m, for this photodetector. Even for the photodetector nearest the interaction site, $\eta_m(\boldsymbol{R})$ tends to be small. For example, the maximum value of $\eta_m(\boldsymbol{R})$ for the camera depicted in Fig. 1 is 6%, which occurs when $\boldsymbol{R}$ is nearest the center of the mth photodetector. From [12], we learn that a low-efficiency binomial selection of scintillation light results in an independent Poisson probability model for each of the M photodetector inputs (photoelectrons), $\boldsymbol{N} = \{N_m | m = 1, \ldots, M\}$. Here, N_m is the number of photoelectrons produced at the input of the mth photodetector. This point is clarified further in [13], where we see that the photoelectron covariance of the m and m' photodetectors is given by:

$$[\boldsymbol{K}_{\boldsymbol{N}}(R, E)]_{mm'} = \bar{N}_{\mathrm{opt}}(E)\eta_m(\boldsymbol{R})\delta_{mm'} + [\mathrm{Var}(N_{\mathrm{opt}}|E) - \bar{N}_{\mathrm{opt}}(E)]\eta_m(\boldsymbol{R})\eta_{m'}(\boldsymbol{R}), \quad (2)$$

where $\bar{N}_{\mathrm{opt}}(E)$ and $\mathrm{Var}(N_{\mathrm{opt}}|E)$ are the mean and variance of the scintillator light yield, N_{opt}, respectively, and $\delta_{mm'}$ is a Kronecker delta. Again, the fraction of scintillation light collected by the mth photodetector, $\eta_m(\boldsymbol{R})$, is a product of geometric and quantum efficiencies of this photodetector. If either the collection or conversion of scintillation light is inefficient, then $[\boldsymbol{K}_N(\boldsymbol{R}, E)]_{mm'} \approx \bar{N}_{\mathrm{opt}}(E)\eta_m(\boldsymbol{R})\delta_{mm'}$ and the photoelectrons in different PMTs are approximately independent and Poisson distributed. The probability model for the photoelectrons in this case is just a product of Poisson distributions (one for each photodetector). For the simulated test camera, we find that the average over $\boldsymbol{R}$ of the largest collection efficiency at each $\boldsymbol{R}$ is 1% and the maximum over all channels and positions is 6%. Furthermore, the average over all channels and over all positions is just 0.1%. For this reason we assume the photodetector inputs are independent and Poisson distributed.

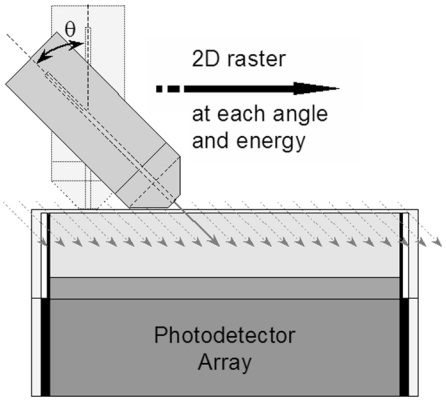

Fig. 2. Acquisition of data for calibrating the detector response statistics as a function of 3D position of interaction. For the current work, the detector response is simulated for an ensemble of gamma rays on a regular 1.52 mm-spaced 2D array of collimator beam positions. Calibration data can also include various gamma-ray beam angles and energies.

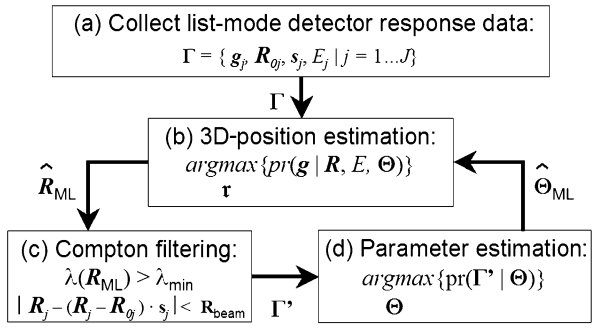

Fig. 3. Procedure for calibrating statistics of the detector response (i.e., $\bar{N}(R, E, \Theta)$) as a function of 3D interaction position. (a) The detector response is measured for an ensemble of gamma rays with known input position, direction, and energy. Event data are initially filtered to keep only photopeak events. (b) An ML estimate of 3D position for each photopeak event is determined. An initial estimate of $\bar{N}$ is made (from 2D MDRF or simulation). (c) Photopeak event data are filtered further by applying a likelihood threshold on 3D-position ML estimate and by using prior knowledge of the collimated beam profile. (d) An ML estimate of Θ is made. Steps (b)–(d) are repeated until a steady-state solution is reached.

C. Electronic Amplification and Readout

To avoid competing with thermal noise in readout electronics, the photodetector input is amplified. For photomultiplier tubes (PMTs), the net gain tends to be large ($\sim 10^6$) and is approximately constant. If electronic and gain noise are negligible (a condition that we presently assume), then the probability model for the output signals, $\boldsymbol{g}$, of a PMT-based scintillation camera is described well as a multivariate scaled-Poisson:

$$\mathrm{pr}(\boldsymbol{g}|\boldsymbol{R}, E) = \prod_{m=1}^{M} \bar{N}_m^{N_m} e^{-\bar{N}_m}/N_m!, \quad \text{where}$$
$$N_m \equiv u(g_m/G_m), \text{ and } \bar{N}_m \equiv \langle g_m(\boldsymbol{R}, E)\rangle/G. \qquad (3)$$

Here, $\langle\cdots\rangle$ is an ensemble average, and $u(\cdots)$ is a rounding operator. There are a total of M photodetectors (channels). For the mth photodetector, G_m is the channel gain, N_m is the number of input photoelectrons, and $\bar{N}_m \equiv \bar{N}_m(\boldsymbol{R}, E)$ is the mean of N_m for given $\boldsymbol{R}$ and E; we omit the functional dependence on $\boldsymbol{R}$ and E here as a notational convenience. We often refer to the vector $\bar{\boldsymbol{N}} \equiv \{\bar{N}_m, m = 1\mathsf{K}\cdots M\}$ as the mean detector response function (MDRF). Hence, to characterize $\mathrm{pr}(\boldsymbol{g}|\boldsymbol{R}, E)$, we only need to determine G_m and $\bar{N}_m$ for each photodetector.

III. Calibrating Gains

We can include gains, $\boldsymbol{G} \equiv \{G_m, m = 1\cdots M\}$, as additional unknown parameters in our calibration of $\bar{\boldsymbol{N}}$ (see Section IV). Alternatively, we can use a separate method to calibrate $\boldsymbol{G}$; for example, we can examine the pulse height spectrum of one or a few photoelectrons (e.g., see [14]), or we can use the variance-to-mean ratio for a scaled-Poisson signal distribution (e.g., see Section 5.2.4 in [8]). We presently choose unit gains and we assume these gains have been separately calibrated.

IV. Calibrating $\bar{\boldsymbol{N}}$

To calibrate the 3D MDRF, we choose a parametric representation such as a set of polynomials (see Section V) and then we estimate the parameters for this representation. Let $\boldsymbol{\Theta} \equiv \{\Theta_i, i = 1\cdots I\}$ be a set of parameters representing the mean detector response functions for the M photodetectors, $\bar{\boldsymbol{N}} \equiv \bar{\boldsymbol{N}}(\boldsymbol{R}, E, \boldsymbol{\Theta})$. The data from which we want to estimate the parameters is the set of observations, $\boldsymbol{\Gamma} \equiv \{\boldsymbol{\gamma}_j, j = 1\cdots J\}$, for J events produced using a collimated gamma-ray source to control the position and orientation of incident gamma rays (Fig. 2). Observations $\boldsymbol{\gamma}_j$ for the jth gamma ray consist of the camera signals $\boldsymbol{g}_j \equiv \{g_{mj}, m = 1\cdots M\}$ and event tags specifying the 2D beam position $\boldsymbol{R}_{0j}$, the beam orientation $\boldsymbol{s}_j$, and the gamma-ray energy E_j. Thus, we calibrate $\bar{\boldsymbol{N}}$ by estimating the parameters $\boldsymbol{\Theta}$ that maximize $\mathrm{pr}(\boldsymbol{\Gamma}|\boldsymbol{\Theta})$ for given list-mode data $\boldsymbol{\Gamma}$:

$$\hat{\boldsymbol{\Theta}}_{\mathrm{ML}} = \arg\max_{\boldsymbol{\Theta}}\{\mathrm{pr}(\boldsymbol{\Gamma}|\boldsymbol{\Theta})\} = \arg\max_{\boldsymbol{\Theta}}\{\ln[\mathrm{pr}(\boldsymbol{\Gamma}|\boldsymbol{\Theta})]\}. \quad (4)$$

Since the camera signals for different gamma-ray events are independent, $\mathrm{pr}(\boldsymbol{\Gamma}|\boldsymbol{\Theta})$ can be factored as:

$$\mathrm{pr}(\boldsymbol{\Gamma}|\boldsymbol{\Theta}) = \prod_{j=1}^{J} \mathrm{pr}(\gamma_j|\boldsymbol{\Theta}). \qquad (5)$$

From this result, the log-likelihood can conveniently be expressed as a sum of log-likelihoods for each event. Furthermore, since $\boldsymbol{R}_{0j}$, and $\boldsymbol{s}_j$ are known experimentally and E_j is assumed to be a fixed deposited energy for each event, we can write:

$$\mathrm{pr}(\gamma_j|\boldsymbol{\Theta}) = \mathrm{pr}(\boldsymbol{g}_j|\boldsymbol{R}_{0j}, \boldsymbol{s}_j, E_j, \boldsymbol{\Theta}). \qquad (6)$$

We now can relate $\mathrm{pr}(\boldsymbol{g}_j|\boldsymbol{R}_{0j}, \boldsymbol{s}_j, E_j, \boldsymbol{\Theta})$ to the 3D probability model $\mathrm{pr}(\boldsymbol{g}_j|\boldsymbol{R}_j, E_j, \boldsymbol{\Theta})$ by accounting for the randomness in pathlength, L. Given that $\boldsymbol{R}_j = \boldsymbol{R}_{0j} + \boldsymbol{s}_j L$, and if we have prior knowledge of the pathlength distribution $\mathrm{pr}(L|E_j, \boldsymbol{R}_{0j}, \boldsymbol{s}_j)$, we express $\mathrm{pr}(\boldsymbol{g}_j|\boldsymbol{R}_{0j}, \boldsymbol{s}_j, E_j, \boldsymbol{\Theta})$ as:

$$\mathrm{pr}(\boldsymbol{g}_j|\boldsymbol{R}_{0j}, \boldsymbol{s}_j, E_j, \boldsymbol{\Theta}) = \int_0^\infty dL\, \mathrm{pr}(\boldsymbol{g}_j|\boldsymbol{R}_j, E_j, \boldsymbol{\Theta})\, \mathrm{pr}(L|E_j, \boldsymbol{R}_{0j}, \boldsymbol{s}_j). \quad (7)$$

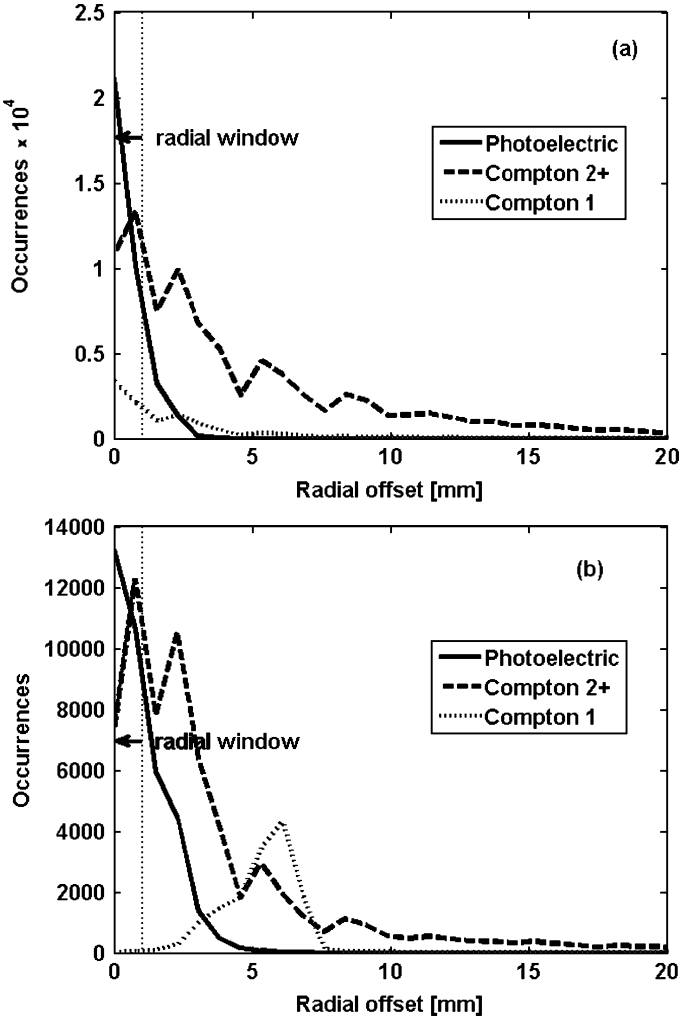

Fig. 4. Radial distributions about calibration-beam axis of 3D-position estimates for (a) camera center and (b) camera corner. We show these distributions for three types of interaction events: photoelectric primary (Photoelectric), Compton primary with one or more secondary interactions (Compton 2+), and Compton primary with secondary escape (Compton 1). The fraction of events within a 1-mm radial window about the beam axis is 51% and 55%, respectively.

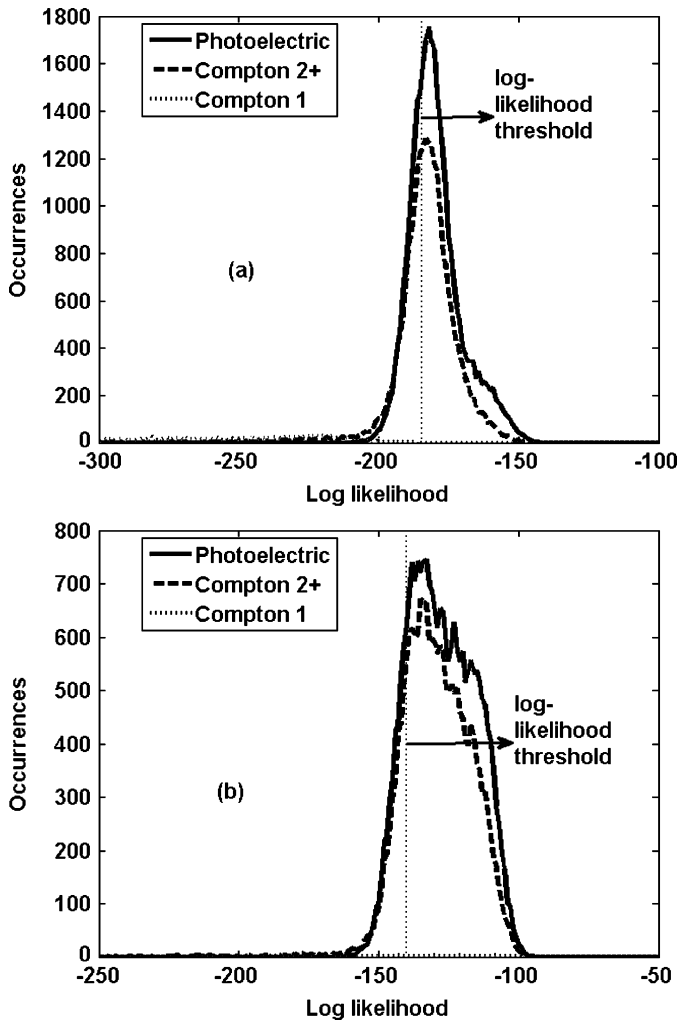

Fig. 5. We show likelihood distributions for three types of interaction events whose position estimates are within 1 mm of calibration-beam axis: photoelectric primary (Photoelectric), Compton primary with one or more secondary interactions (Compton 2+), and Compton primary with secondary escape (Compton 1). Results are shown for a calibration beam at (a) the camera center and (b) camera corner. The fraction of filtered events that are photoelectric at these two positions is 60% and 55%, respectively. In each case, less than 1% of filtered events are Compton primary events with secondary escape (dotted curves for the Compton-1 case appear near the bottom of each plot).

The pathlength distribution here generally depends on the photon energy, input position, and direction (see Section VII). Making use of (4)–(7), we can then express $\ln[\mathrm{pr}(\mathbf{\Gamma}|\mathbf{\Theta})]$ as:

$$\ln[\mathrm{pr}(\mathbf{\Gamma}|\mathbf{\Theta})] = \sum_{j=1}^{J} \ln\left[\int_0^\infty dL\, \mathrm{pr}(L|E_j, \mathbf{R}_{0j}, \boldsymbol{s}_j) \exp\left(\sum_{m=1}^{M} \Lambda_{\mathrm{mj}}\right)\right] - \mathbb{C}, \tag{8}$$

where, for a multivariate scaled-Poisson (3), we have:

$$\Lambda_{mj} \equiv N_{mj}\, \ln[\bar{N}_m(\boldsymbol{R}_j, E_j, \mathbf{\Theta})] - \bar{N}_m(\boldsymbol{R}_j, E_j, \mathbf{\Theta}),$$
$$\mathbb{C} \equiv \sum_{j=1}^{J}\sum_{m=1}^{M} \ln(N_{mj}!), \text{ and } \boldsymbol{R}_j = \boldsymbol{R}_{0j} + \boldsymbol{s}_j L. \tag{9}$$

Since $\bar{\boldsymbol{N}}$ scales with the average amount of light produced by a gamma-ray interaction, we are able to relate the MDRF at different energies. With knowledge of the average energy dependence of scintillator light yield $f(E)$ (as in [15]), we can separate the energy dependence of $\bar{\boldsymbol{N}}$:

$$\bar{\boldsymbol{N}}(\boldsymbol{R}, E, \mathbf{\Theta}) = \bar{\mathbb{N}}(\boldsymbol{R}, \mathbf{\Theta}) f(E). \tag{10}$$

We can then use multiple gamma-ray energies to calibrate just the spatial dependence of the MDRF, $\bar{\mathbb{N}}(\boldsymbol{R}, \mathbf{\Theta})$. Different gamma-ray energies result in different gamma-ray pathlength distributions, $\mathrm{pr}(L|E_j, \boldsymbol{R}_{0j}, \boldsymbol{s}_j)$, and hence result in different contributions to the likelihood for the list-mode data (i.e., see (8)). By including multiple gamma-ray energies as part of our list-mode data, $\mathbf{\Gamma}$, we increase the information available for calibrating just the spatial dependence of the MDRF, $\bar{\mathbb{N}}(\mathbf{R}, \mathbf{\Theta})$.

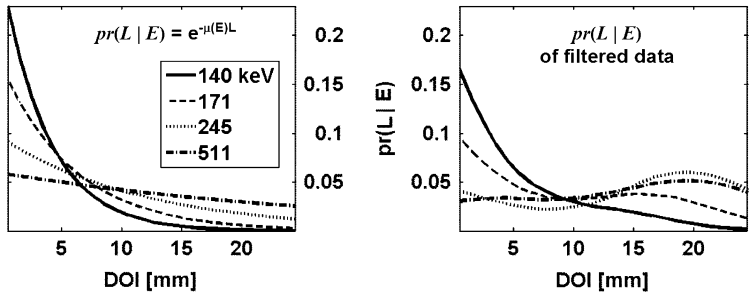

Fig. 6. Probability density of pathlength for normally incident gamma rays at the test camera center: (left) all gamma rays, and (right) filtered gamma rays. Events are filtered using a radial window of 1 mm about the beam axis and a likelihood threshold that retains a constant fraction of events equal to the photoelectric branching ratio.

V. Parametric Representation of $\bar{\mathbb{N}}(\boldsymbol{R}, \boldsymbol{\Theta})$

Various choices of $\boldsymbol{\Theta}$ exist. For example, we can use a regular array of discrete samples (voxels). Another approach is to use a physical model for light propagation with several free parameters. Alternatively, since $\bar{\mathbb{N}}(\boldsymbol{R}, \boldsymbol{\Theta})$ should vary smoothly with $\boldsymbol{R}$, we may choose $\boldsymbol{\Theta}$ as the set of parameters for an analytic form (e.g., see [16]).

For the results that follow, we use a hybrid representation, fitting the mean detector response continuously as a function of depth for a discrete set of lateral positions. For the mth photodetector and a lateral position (x, y), we fit the response as a function of depth with a cubic polynomial:

$$\bar{\mathbb{N}}_m(\boldsymbol{R}, \boldsymbol{\Theta}) = \sum_{n=0}^{3} c_{mn}(x,\, y) z^n, \tag{11}$$

where parameters, $\boldsymbol{\Theta}$, describe the coefficients, $c_{mn}(x, y)$, as a function of lateral position. As will become apparent, we simplify the task of optimizing $\boldsymbol{\Theta}$ in (8) by representing $c_{mn}(x, y)$ with a regular 2D-array of samples. We choose these lateral positions such that the 3D-MDRF can be accurately interpolated at any point in the detector volume.

To estimate parameters in this representation, we assume K normally oriented calibration-beam positions. The parameters for each beam position, $c_{mn}(x_k, y_k)$, form a set of K matrices, $\boldsymbol{c}_k$, $M \times 4$ each, where M is the number of photodetectors. ML estimation of $\boldsymbol{\Theta}$ in this case conveniently separates into K optimization problems of $M \times 4$ parameters each:

$$\hat{c}_k = \arg\max_{\boldsymbol{c}_k} \{\mathrm{pr}(\boldsymbol{\Gamma}_k | \boldsymbol{c}_k)\}. \tag{12}$$

To maintain separability of parameters for the optimization task, we choose not to use multiple calibration-beam angles.

VI. Filtering Multiple Interactions

We must filter multiple-interaction events to calibrate $\bar{\boldsymbol{N}}$ for single interactions. We do so by using prior knowledge of the calibration beam position and beam profile and by applying a threshold on the prior-weighted likelihood of the 3D-position ML estimate for each gamma ray.

The estimated position of a photoelectric primary is likely to be closer to the beam axis than is the position estimate for a Compton interaction. The Compton secondary interaction often occurs away from the beam axis, which similarly affects the position estimate. Making use of this information, we weight the likelihood of the ML position estimate for an event by the prior of its radial offset from the calibration beam axis. Events are then filtered using a threshold on this prior-weighted likelihood. For this work, we assume the beam profile is a uniform circular disk. The event filter in this case is equivalent to keeping events that are estimated within a distance R_{beam}, of the beam center $\boldsymbol{R}_o$ and that pass a likelihood threshold; see step (c) in Fig. 3.

To produce a 3D-position estimate for each event, we need an initial estimate of the 3D MDRF, $\bar{\boldsymbol{N}}$. For an experimental calibration, a simulated 3D MDRF can serve as an initial estimate of $\bar{\boldsymbol{N}}$. However, to avoid biasing our results for this simulation study, we use the 2D MDRF, which is marginalized over depth, and we assume no depth sensitivity. In either case, we then refine our estimate of $\bar{\boldsymbol{N}}$ by maximizing $\mathrm{pr}(\boldsymbol{\Gamma}|\boldsymbol{\Theta})$ given the remaining events after filtering multiple-interaction events. We iterate this process of event filtering and estimation of $\boldsymbol{\Theta}$ until a steady-state solution is reached (Fig. 3).

In this work, we assume a uniform radial density out to a radius of 1.0 mm; events that are estimated to be beyond 1.0 mm of the calibration beam axis are removed. In addition, we choose a likelihood threshold for each beam position such that the fraction of events kept is equal to the photoelectric branching ratio for a gamma-ray interaction of known energy. Figs. 4 and 5 give an example of this filtration process for 511-keV gamma rays.

VII. Pathlength Distribution

In a homogeneous detector, we expect gamma-ray pathlength to be exponentially distributed. However, due to imperfect filtering of multiple interaction events, the pathlength distribution of the calibration data is not given by Beer's law as expected. Rather, this distribution depends on the detector geometry, the gamma-ray energy, direction and entrance position, and the specific event filter being used. We rely on simulation to determine $\mathrm{pr}(L|\boldsymbol{R}_{0j}, \boldsymbol{s}_j, E_j)$ for a specific detector and filter; see Fig. 6.

VIII. Results of a Simulated Calibration

We performed Monte-Carlo (MC) simulations of gamma-ray interaction, light yield, and optical transport in the test camera design shown in Fig. 1 using the SCOUT simulation tool reported in [8]. A 25-mm-thick, 52-mm-wide square block of NaI(Tl) is optically coupled to the borosilicate window of a Hamamatsu H8500 (an 8-by-8 MA-PMT) [17]. The NaI(Tl) entrance and edge surfaces are treated as ideal retroreflectors

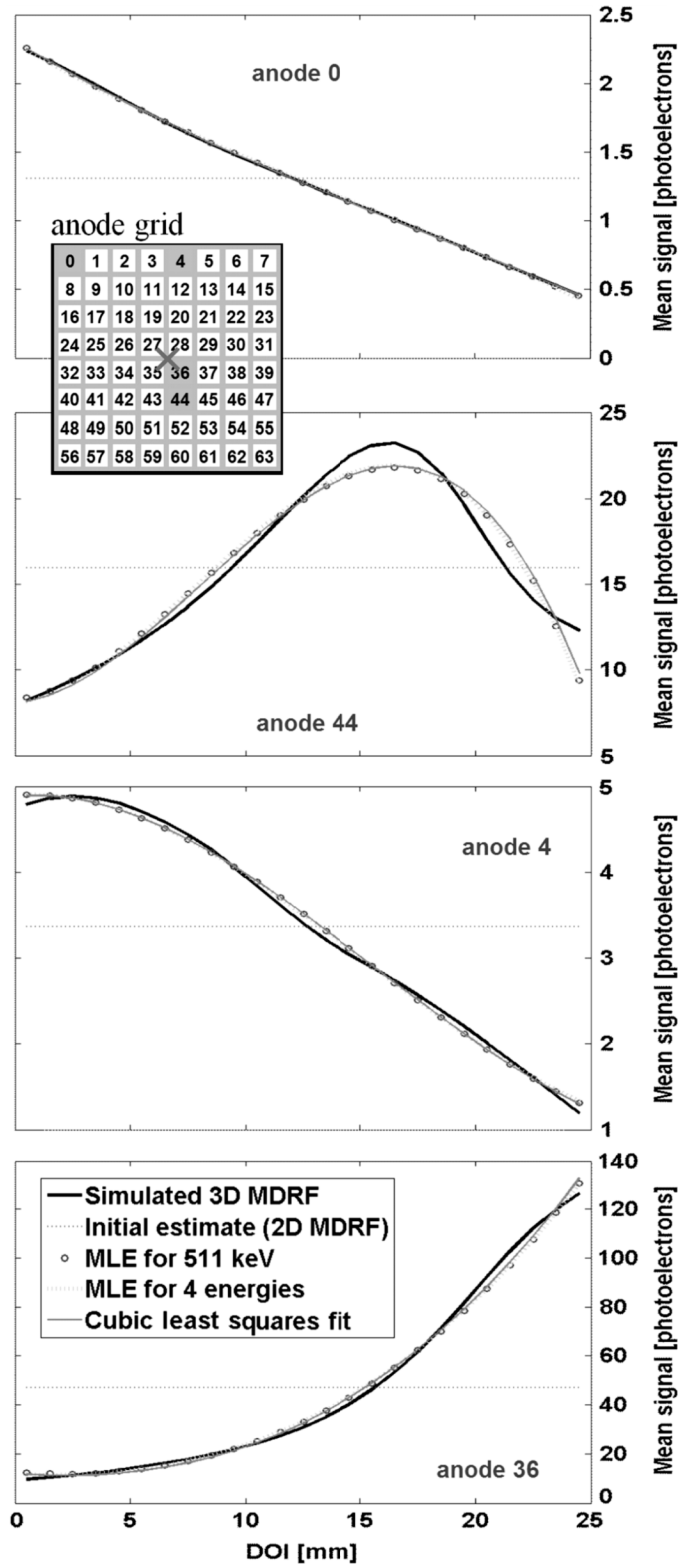

Fig. 7. Profile of true vs. ML estimate of $\bar{N}$ as a function of depth (z) for several anodes with interactions through the camera center ($x = y = 0$). The position of these anodes and the lateral interaction position in this case are indicated in the anode grid shown near the top of this figure. The accuracy of fit is similar for other anodes and other positions. The estimate of $\bar{N}$ approximates the cubic least squares fit in each case.

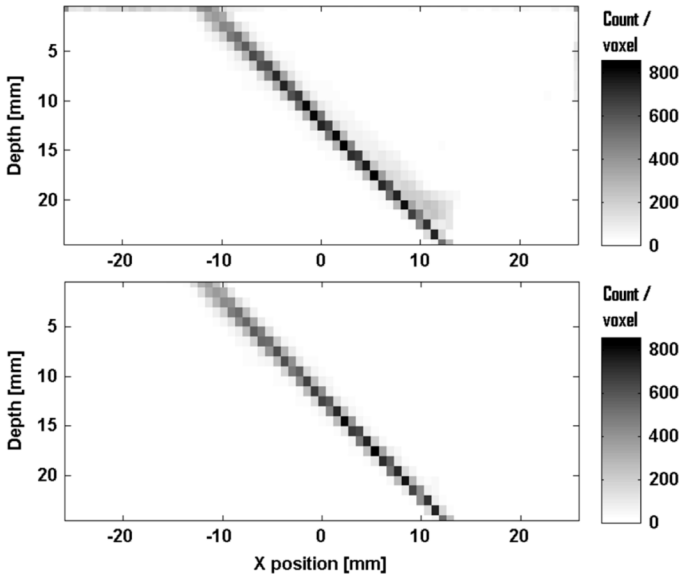

Fig. 8. Cross section ($y = 0$) of 3D ML-estimate distribution for a perfectly collimated 45°-slanted 511 keV gamma-ray beam using the 4-energy ML estimate for $\bar{N}$: (top) estimate distribution for all events, (bottom) a likelihood threshold is used to remove events not likely to be primary photoelectric interactions.

with 95% reflectance. The NaI(Tl) interface with the MA-PMT window is treated as a micro-faceted diffuse interface; the slopes of individual facets of this surface are normally distributed about the surface mean with a variance of 0.01. The H8500 MA-PMT has a bialkali photocathode that we model as having a complex refractive index of $3.4 - \mathrm{i}2.2$ for wavelengths near 410 nm and we model a spectrally averaged quantum efficiency (QE) of 23.1%. We use the scintillation spectrum for NaI(Tl) reported by [18] to weight the spectral QE for this photodetector. The refractive indices of NaI(Tl) and borosilicate glass are taken to be 1.850 and 1.469, respectively. Amplification noise and electronic noise were assumed negligible for this simulation.

Making use of the filtering and calibration methods described above, we produced an estimate of $\bar{N}$ for this simulated camera design. We examined two cases: use of just 511 keV gamma rays and use of a combination of 4 energies: 140, 171, 245, and 511 keV. All gamma rays are assumed to be at normal incidence. For each case, we sought the ML estimate of $\bar{N}$ using a conjugate gradient search algorithm.

Representative results for these calibrations of $\bar{N}$ are shown in Fig. 7. The 3D-MDRF was calibrated on a 1.52-mm grid of beam positions. Interpolating the calibrated 3D-MDRF to a 0.76-mm lateral grid, we then generated 3D-position estimates for simulated 511 keV gamma-ray interactions of a perfectly collimated 45°-slanted beam (shown in Fig. 8). To reject events not likely to have been produced under the assumed signal probability model and to improve estimate variance, we applied a threshold on the estimate likelihood. For the simulated test-camera, resolution of interaction position is on the order of the estimate grid size (0.76 mm).

To measure detector spatial resolution as a function of position, we can interpolate the MDRF and image a slant-beam at different positions in the detector. Alternatively, for an ML estimator, we can compute bounds on detector spatial-resolution predicted by Fisher information theory [6]–[8]. In Fig. 9, we show Cramér-Rao (CR) bounds on lateral resolution and depth

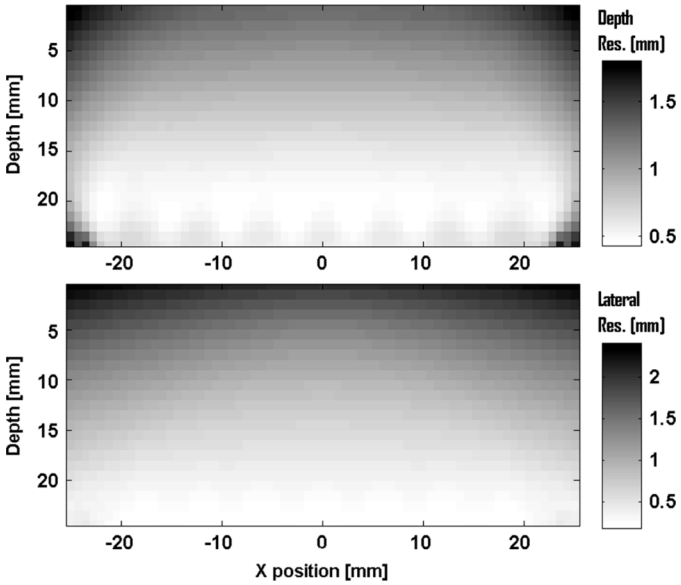

Fig. 9. Vertical cross section ($y = 0$) of the Cramér-Rao (CR) bound on detector resolution of (top) depth and (bottom) lateral position for a single 511 keV gamma interaction in the test camera (Fig. 1). Our measure of resolution is the full-width at half-max computed as $2\,[2\ln(2)[\boldsymbol{F}^{-1}]_{jj}]^{1/2}$, where $[\boldsymbol{F}^{-1}]_{jj}$ is the CR bound on variance for the jth parameter estimate.

resolution of 511 keV gamma rays interacting in the test camera. Our measure of resolution is the full-width at half-max computed as $2\,[2\ln(2)[\boldsymbol{F}^{-1}]_{jj}]^{1/2}$, where $[\mathbf{F}^{-1}]_{jj}$ is the CR bound on variance for the jth parameter estimate. We compute CR bounds here, as is done in [19], using a multivariate Poisson probability model conditioned on interaction position and energy for the number of detected optical photons in each of the photodetectors.

IX. Discussion

By maximizing the list-mode likelihood, $\mathrm{pr}(\boldsymbol{\Gamma}|\boldsymbol{\Theta})$, with prior knowledge of pathlength distribution, we are able to accurately calibrate detector-response statistics as a function of 3D position of interaction in a gamma camera. Accuracy of the 3D-MDRF calibration for the case considered was limited primarily by the parametric representation chosen; we see in Fig. 7 that the least squares fit of a cubic polynomial to the known MDRF is closely reproduced by the ML fit. Finally, we found that use of multiple gamma-ray energies did not significantly improve calibration accuracy. However, this latter conclusion may depend on the number of events used to perform the calibration.

Making use of the calibrated 3D-position likelihood model, we have then shown how to estimate the 3D interaction position. We reject events not likely to have been produced under the assumed signal probability model by applying a threshold on estimate likelihood. An optimal choice of likelihood threshold for imaging a living patient is best determined by task-based assessment of image quality (a topic left for future work). However, for simulated imaging, we can choose a fairly restrictive likelihood threshold. In Fig. 8, we find the resulting 3D-position estimates to be unbiased, which suggests that the ML fit of the 3D-MDRF is sufficiently accurate for this purpose. The Cramér-Rao bound on spatial resolution at 511 keV for the simulated test-camera design (Fig. 1) was determined to be sub-millimeter for most of the detector volume in both lateral and depth dimensions.

The detector model we have used to illustrate the list-mode maximum likelihood (LMML) calibration method is inaccurate in some ways that may affect the detector resolution shown in Fig. 9. Specifically, we recognize that the retroreflector model we used is ideal. We have since developed more detailed models for real retroreflectors, but we did not implement these for the purposes of this paper, which are to illustrate and validate the LMML calibration procedure. Furthermore, we find that the advantage gained by an ideal (as opposed to real) retroreflector can be realized equivalently by using newer scintillators with more light output or newer photocathodes with higher QE; these two advances suggest that even better performance should be attainable even without retroreflectors.

Another place where the simulated detector might be inaccurate is in modeling scintillator-PMT interface reflections [20]. For this work, we have used a spatially invariant micro-faceted surface model with normally distributed slopes [8]. If we address this point more accurately, then we might slightly change our prediction of real-world performance in an undetermined way (for better or for worse). Either way, we are likely to see better performance (in terms of estimate resolution and bias) when using the calculated response function for position estimation. To this end, we have successfully demonstrated a method for calibrating detector response as a function of 3D interaction position, independent of the simulation model.

The LMML calibration method we have examined for calibrating detector response as a function of 3D interaction position can be used with an arbitrary detector design. However, we find the LMML method of particular importance for monolithic (continuous) detectors. Use of side illumination to directly control interaction depth may be more appropriate for calibrating the 3D response function of arrayed scintillation detectors with one-to-one photodetector coupling (e.g., see [2]), but is less effective for a monolithic detector (e.g., see [3]). Several methods exist for encoding more depth information in a detector's response such as phoswich [21], 3D arrays [22], [23], or dMiCE [24], but all require more complex detector fabrication and most of these are capable of only a few depth-resolution elements.

We finish by contrasting the method we've examined to another ML calibration method examined by Ling, *et al.* [5]; a direct comparison of these methods requires knowledge of the calibration bias resulting from each method, but this information is not available directly from [5]. Instead, we elucidate several fundamental distinctions of these methods. First, the LMML method makes no assumption regarding how detector response varies with depth in order to partition interaction depth of individual events; the LMML method relies only on prior knowledge of pathlength distribution. Second, we represent response as a function of depth continuously and we estimate parameters of this representation using events from all depths. Finally, we filter multiple-interaction events from the calibration data by windowing the likelihood of their position estimates weighted by the prior on the calibration beam profile.

X. Outlook

Experimental calibration of detector-response statistics as a function of 3D interaction position is an area of future work. Preliminary experimental results using a related calibration method are reported in [25]. In this related work, a locally scaled solid-angle model is used to parametrically represent the 3D MDRF; scaling coefficients are then chosen to fit the observed spectra for normal calibration-beam data.

The use of list-mode likelihood for calibration of response statistics as a function of 3D position was demonstrated for a continuous-scintillator gamma camera, but is generally applicable for other camera types and geometries. For instance, list-mode calibration of detector response statistics with DOI can similarly be applied to segmented detectors. However, in this case, the detector response is discontinuous across segment boundaries. Therefore, the parametric representation of the MDRF that we use should reflect this fact. Calibration of each detector segment can be performed independently.

This calibration method can also be extended for use with different signal probability models. For instance, if gain noise is not negligible (i.e., as for avalanche photodiodes), then we might instead use an independently distributed (i.d.) multivariate normal probability model (see Section 3.3.5 in [8]). In this case, we must simultaneously calibrate the mean and variance of the detector response as a function of 3D position. The general procedure we have proposed to calibrate the mean response can also be used to calibrate the response variance; to do so, we would require more data to simultaneously calibrate the additional statistics.

Having adequately calibrated the detector response for single interactions, we can mitigate issues of parallax and signal variance due to random interaction depth. The topic of multiple-interaction parameter estimation is another area of work that can be expanded upon once we can adequately calibrate the detector response for single interactions (see Section 3.3.6 of [8]).

References

[1] D. Gagnon, N. Pouliot, L. Laperrikre, M. Therrien, and P. Olivier, "Maximum likelihood positioning in the scintillation camera using depth of interaction," *IEEE Trans. Med. Imag.*, vol. 12, no. 1, pp. 101–107, Jan. 1993.

[2] A. Ivan, K. C. Burr, Y. Shao, and J. W. LeBlanc, "Depth of interaction effect on timing resolution in PET block detectors," in *Proc. Nucl. Sci. Symp. Conf. Rec.*, 2004, vol. 7, pp. 4156–4158.

[3] C. W. Lerche, J. M. Benlloch, F. Sánchez, N. Pavón, B. Escat, E. N. Gimenez, M. Fernández, I. Torres, M. Giménez, A. Sebastià, and J. Martínez, "Depth of γ-ray interaction within continuous crystals from the width of its scintillation light-distribution," *IEEE Trans. Nucl. Sci.*, vol. 52, no. 3, pp. 560–572, Jun. 2005.

[4] J. Seidel, J. J. Vaquero, S. Siegel, W. R. Gandler, and M. V. Green, "Depth identification accuracy of a three-layer phoswich PET detector module," *IEEE Trans. Nucl. Sci.*, vol. 46, no. 3, pp. 485–490, Jun. 1999.

[5] T. Ling, T. K. Lewellen, and R. S. Miyaoka, "Depth of interaction decoding of a continuous crystal detector module," *Phys. Med. Bio.*, vol. 52, pp. 2213–2228, 2007.

[6] H. H. Barrett and K. J. Myers, *Foundations of Image Science*. New York: Wiley, 2004.

[7] L. R. Furenlid, J. Y. Hesetrman, and H. H. Barrett, "Real-time data acquisition and maximum-likelihood estimation for gamma cameras," presented at the 14th IEEE-NPSS Real Time Conf. Rec., Stockholm, Sweden, 2005.

[8] W. C. J. Hunter, "Modeling stochastic processes in gamma-ray imaging detectors and evaluation of a multi-anode PMT scintillation camera for use with maximum-likelihood estimation methods," Ph.D. dissertation, Dept. Phys., Univ. Arizona, Tucson, 2007.

[9] J. D. Valentine, B. D. Rooney, and J. Li, "The light yield nonproportionality component of scintillator energy resolution," *IEEE Trans. Nucl. Sci.*, vol. 45, no. 3, pp. 512–517, Jun. 1998.

[10] M. J. Weber, "Scintillation: Mechanisms and new crystals," *Nucl. Instr. Meth. Phys. Res. A*, vol. 527, pp. 9–14, 2004.

[11] W. W. Moses, "Current trends in scintillator detectors and materials," *Nucl. Instr. Meth. Phys. Res. A*, vol. 487, pp. 123–128, 2002.

[12] H. H. Barrett, "Detectors for small-animal SPECT II: Statistical limitations and estimation methods," in *Small-Animal SPECT Imaging*. New York: Springer, 2005, ch. 3.

[13] H. H. Barrett and W. Swindell, *Radiological Imaging: Theory of Image Formation, Detection and Processing, Volume I and II*. New York: Academic, 1981.

[14] R. W. Engstrom, "Photomultiplier handbook," Burle Industries, Inc., Lancaster, PA, 1989.

[15] B. D. Rooney and J. D. Valentine, "Scintillator light yield nonproportionality: Calculating photon response using measured electron response," *IEEE Trans. Nucl. Sci.*, vol. 44, no. 3, pp. 509–516, Jun. 1997.

[16] T. Tomitani, Y. Futami, Y. Iseki, S. Kouda, T. Nishio, T. Murakami, A. Kitagawa, M. Kanazawa, E. Urakabe, M. Shinbo, and T. Kanai, "Depth encoding of point-of-interaction in thick scintillation cameras," in *Proc. Nucl. Sci. Symp. Conf. Rec.*, 1999, vol. 3, pp. 1182–1186.

[17] Hamamatsu Photonics K. K., "Flat panel type multianode photomultiplier tube assembly," Hamamatsu Photonics K. K., Iwata, Japan, 2006.

[18] J. Sain, "Optical modeling, design optimization, and performance analysis of a gamma camera for detection of breast cancer," Ph.D. dissertation, College Opt. Sci., Univ. Arizona, Tucson, 2001.

[19] D. J. van der Laan, M. C. Maas, D. R. Schaart, P. Bruyndonckx, S. Léonard, and C. W. E. van Eijk, "Using Cramer-Rao theory combined with Monte-Carlo simulations for the optimization of monolithic scintillator PET detectors," *IEEE Trans. Nucl. Sci.*, vol. 53, no. 3, pp. 1063–1070, Jun. 2006.

[20] I. V. Kilimchuk, V. A. Tarasov, and J. M. Alameda, "Study of surface roughness of CsI:Tl crystals treated by various abrasives," in *Proc. Nucl. Sci. Symp. Conf. Rec.*, 2008, pp. 1134–1137.

[21] D. H. Wilkinson, "The Phoswich—A multiple phosphor," *Rev. Sci. Instr.*, vol. 23, pp. 414–417, 1952.

[22] T. Yamashita, M. Watanabe, K. Shimizu, and H. Uchida, "High resolution block detectors for PET," *IEEE Trans. Nucl. Sci.*, vol. 37, no. 2, pp. 589–593, Mar. 1990.

[23] H. Liu, T. Omura, M. Watanabe, and T. Yamashita, "Development of a depth of interaction detector for γ-rays," *Nucl. Instr. Meth. Phys. Res. A*, vol. 459, pp. 182–190, 2001.

[24] T. K. Lewellen, L. R. MacDonald, R. S. Miyaoka, W. McDougald, and K. Champley, "New directions for dMiCE—A depth-of-interaction detector design for PET scanners," in *Proc. Nucl. Sci. Symp. Conf. Rec.*, 2007, vol. 5, pp. 3798–3802.

[25] S. K. Moore, W. C. J. Hunter, L. R. Furenlid, and H. H. Barrett, "Maximum-likelihood estimation of 3D event position in monolithic scintillation crystals: Experimental results," in *Proc. Nucl. Sci. Symp. Conf. Rec.*, 2007, vol. 5, pp. 3691–3694.